### Title

An Epsilon-Near-Zero Total-Internal-Reflection Metamaterial Antenna




### Journal

IEEE Transactions on Antennas and Propagation, 63(5)

### ISSN

0018-926X



### Authors

Forati, Ebrahim
Hanson, George W
Sievenpiper, Dan F



### Publication Date

2015-05-01

### DOI

10.1109/tap.2015.2405559

Peer reviewed

# An Epsilon-Near-Zero Total-Internal-Reflection Metamaterial Antenna

Ebrahim Forati, *Graduate Student Member, IEEE*, George W. Hanson, *Fellow, IEEE*, and Dan F. Sievenpiper, *Fellow, IEEE*

***Abstract*—The total-internal-reflection (TIR) principle and the concept of an epsilon-near-zero (ENZ) material are combined to form an antenna exhibiting sum and difference patterns with good impedance properties. The ENZ material has been realized using a uniaxial wire medium (WM) metamaterial, and the departure from the behavior of an ideal ENZ material is discussed. The radiation pattern of the fabricated antennas has been measured and compared with simulation results.**

***Index Terms*—Antenna, epsilon-near-zero, radiation pattern, total internal reflection (TIR), wire medium (WM).**

## I. Introduction

BESIDES being the operating principle of optical fibers, the total internal reflection (TIR) has numerous other applications at optical frequencies such as in microscopes [1] and in spatial filtering of light [2]. Although less popular than at optical frequencies, TIR also has applications at microwave frequencies. Dielectric waveguides [3], dielectric resonators [4], and long distance communication based on ionospherical TIR [5] are among a host of important applications. The TIR law, which is a special case of Snell's law, can be extracted from classical electromagnetic theory quite easily. Based on TIR, if the incident angle of a TM wave on a boundary is larger than the critical angle, the wave will be totally reflected. This is similar to the case in which a TM wave impinges on a PEC boundary. However, the two cases are different in the phase shift of the reflected electric field, as clarified in Fig. 1. Reflection from a PEC boundary preserves the phase of the magnetic component of a TM wave. In contrast, TIR adds 180° phase change to the magnetic component of a TM wave. This phase shift difference is crucial to the antenna design described here.

ENZ materials are shown to have interesting applications, such as increasing transmission through a subwavelength narrow aperture [6], increasing the directivity of emission from a source [7], [8], and tailoring the radiation pattern of radiators [9]. Scattering from and propagation in ENZ materials are studied in [10]. In an ideal ENZ material, the phase velocity of a plane wave is infinite. As a result, picturing a ray model of radiation, if a radiator is placed inside an ideal ENZ material, the rays emerging from different points of the ENZ boundary are in phase [see Fig. 2(b)]. An alternative explanation of the beam shaping property of an ENZ material is possible by considering Snell's law. Since the critical angle for TIR from an ENZ material boundary is zero, a ray can only emerge from its boundary normally. This phenomenon is also of great importance in our proposed geometry.

Several antennas have been designed using ENZ metamaterial properties [11]–[15]. In [16], the beam forming property of a slab of metamaterial with a small permeability (rather than the permittivity) is studied. In [17], the pattern of a monopole antenna is shaped by immersing it in a uniaxial wire medium (WM) acting as an ENZ material.

A common method to realize ENZ materials is to use a plasma or a material which effectively behaves as a plasma. Noble metals and semiconductors below optical frequencies can be described by a plasma model, although loss is a big limiting factor for metals. At microwave frequencies, a WM is known to implement an artificial plasma, and can be used to realize the ENZ condition. Based on the simple Drude model for permittivity of a plasma [18]–[23],

$$\varepsilon_{\mathrm{r}} = \alpha\left(1 - \frac{\omega_{\mathrm{p}}^2}{\omega\left(\omega - j\Gamma\right)}\right) \tag{1}$$

where $\alpha$ is a constant, $\Gamma$ is the damping frequency, and $\omega_{\mathrm{p}}$ is the plasma frequency. If carriers friction is small (i.e., $\Gamma \ll \omega$), the ENZ condition occurs at the plasma frequency. The equivalent plasma frequency of a uniaxial WM is given as [19]

$$\omega_{\mathrm{p}} \simeq \frac{1}{p\sqrt{\mu_0\varepsilon_0}}\sqrt{\frac{2\pi}{ln\left(\frac{p}{\pi d}\right) + 0.5275}} \tag{2}$$

where $p$ and $d$ are the period and diameter of the WM, respectively (see [19] for exact equations).

However, if the spatial dispersion is included in the WM model, the ENZ condition does not necessarily occur at the plasma frequency given by (2). In general, the ENZ condition is equivalent to having zero electric displacement field inside a material ($\mathbf{D} = 0$). If a material is local,

$$\mathbf{D}\left(\mathbf{r},\omega\right) = \varepsilon\left(\omega\right)\mathbf{E}\left(\mathbf{r},\omega\right) \tag{3}$$

and the ENZ condition will become $\varepsilon = 0$ (which occurs at $\omega_p$ in the case of (1) and $\Gamma \ll \omega$). But, for a spatially dispersive (nonlocal) material such as WM [24]–[26],

$$\mathbf{D}\left(\mathbf{r},\omega\right) = \int \varepsilon\left(\mathbf{r}',\mathbf{r},\omega\right)\mathbf{E}\left(\mathbf{r}',\omega\right)d\mathbf{r}' \tag{4}$$

Manuscript received September 16, 2014; revised January 02, 2015; accepted February 16, 2015. Date of publication February 19, 2015; date of current version May 01, 2015.

E. Forati and D. F. Sievenpiper are with the Department of Electrical and Computer Engineering, University of California, San Diego, CA 92098 USA (e-mail: forati@ieee.org).

G. W. Hanson is with the Department of Electrical and Computer Engineering, University of Wisconsin-Milwaukee, Milwaukee, WI 53202 USA.

Color versions of one or more of the figures in this paper are available online at http://ieeexplore.ieee.org.

Digital Object Identifier 10.1109/TAP.2015.2405559

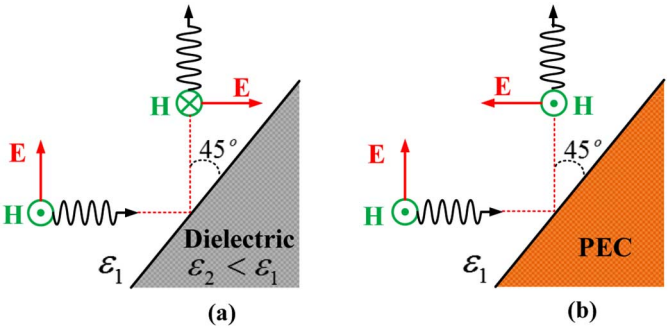


Fig. 1. TM wave incident on: (a) dielectric; and (b) PEC material at a 45° angle. The ratio $\epsilon_2/\epsilon_1$ is assumed small enough to allow total internal reflection.

in which the integration is over the entire space and $\mathbf{r}$ and $\mathbf{r}'$ are the source and the observation coordinates, respectively. It is evident from (4) that the ENZ condition ($\mathbf{D} = 0$) depends on the excitation electric field. The ENZ condition ($\omega_{\mathrm{ENZ}}$) in WM has been discussed with more detail in [24] and it is shown that the exact ENZ condition in isotropic WM can occur with some specific electric field excitations. As such, for a transverse wave traveling inside an isotropic WM (i.e., if the electric field is perpendicular to the propagation direction), the ENZ condition will be realized at [24]

$$\omega_{\mathrm{ENZ}} = \frac{\omega_{\mathrm{p}}}{\sqrt{\varepsilon_{\mathrm{h}}}} \tag{5}$$

where $\varepsilon_{\mathrm{h}}$ is the host permittivity of the wires. Equation (5) is the same ENZ condition as would occur in a local medium independent from the excitation electric field. For longitudinal waves (i.e., the electric filed is parallel to the propagation direction), the ENZ condition in WM will occur at [24]

$$\omega_{\mathrm{ENZ}} = \frac{\omega_{\mathrm{p}}}{\sqrt{\varepsilon_{\mathrm{h}}\left(1 - 1/l_0\right)}} \tag{6}$$

where $l_0$ is a constant between 2 and 3. The radiation properties of an elementary source in a WM are discussed in [27]. These relations will be used in the following to ascertain the ENZ condition.

## II. Proposed Geometry

Fig. 2(a) shows half of the proposed structure. It consists of a rectangular ENZ volume with its upper and lower surfaces covered by PEC (to inhibit direct vertical radiation from the ENZ block). A monopole antenna is placed in the middle of the lower PEC (GND plane) so that it can be easily fed by a coaxial cable. The monopole antennas are chosen for its simplicity and useful radiation pattern. A dielectric flare-shaped non-ENZ dielectric material with 45° side angles surrounds the ENZ block. The permittivity of the dielectric flare is chosen to be large enough so that the critical angle for TIR is less than 45°. Radiation from the monopole exits the ENZ block normal to the block surface (i.e., the ENZ block converts the radiation pattern of the monopole feed to four lateral beams, normal the the side walls of the block), and impinges on the side walls of the flare at a 45° angles and reflects up to the radiating surface, the top

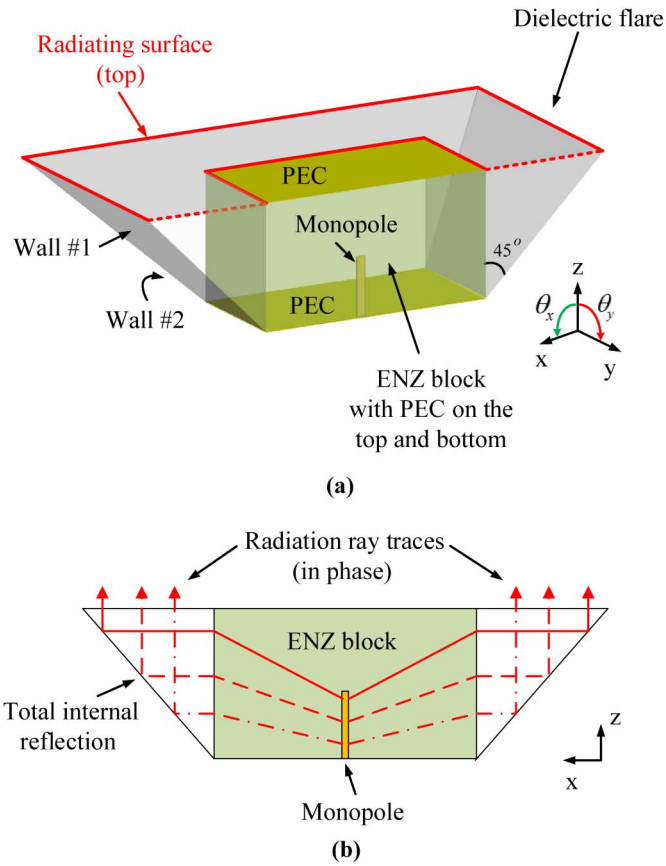


Fig. 2. (a) Half of the proposed antenna geometry. Full geometry will be obtained by adding a mirror image in the $x - z$ plane. (b) $x - z$ view of the geometry showing a ray model of radiation.

surface of the non-ENZ dielectric flare material, as depicted in Fig. 2(b). The ENZ block is necessary to ensure that radiation will impinge on the dielectric flare side walls at a 45° angle. Since the monopole is in the $z$ direction, assuming permittivity is almost zero, Ampere's law simplifies to

$$\nabla \times \mathbf{H} = \mathbf{J} \tag{7}$$

which implies that $H_{\mathrm{z}} = 0$ everywhere inside the ENZ region, assuming a sufficiently long wire. Knowing this and the fact that plane waves can only radiate normally from an ENZ boundary, one can conclude that the electric field is mostly in the $z$ direction. Therefore, the outcoming wave from the ENZ block is a TM wave. Also, the permittivity of the dielectric flare is chosen to be greater than two, which leads to a critical angle less than 45° for TIR at the flare boundary.

The geometry of Fig. 2 will create four beams with a null at $\theta = 0$ (called the difference pattern) as shown in Fig. 3. However, different metalization patterns can be placed on the side walls of the flare to shape the radiation pattern. This is in fact the most important property of this geometry. As a simple example, to generate a single beam (called the sum pattern [28]), two adjacent side walls can be covered by conducting sheets. These side walls have been labeled as #1 and #2 in Fig. 2 and the sum radiation pattern is shown in Fig. 4. In other words, depending on whether edges #1 and #2 are covered with PEC or not, the electric field distribution on the radiating edge is as

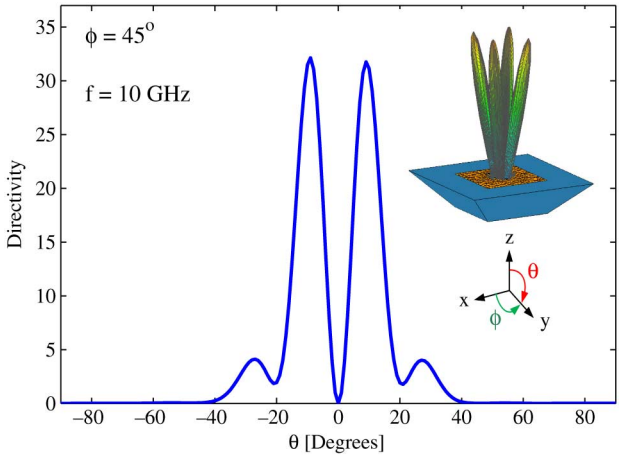


Fig. 3. Simulated directivity of the difference pattern assuming an ideal ENZ block.

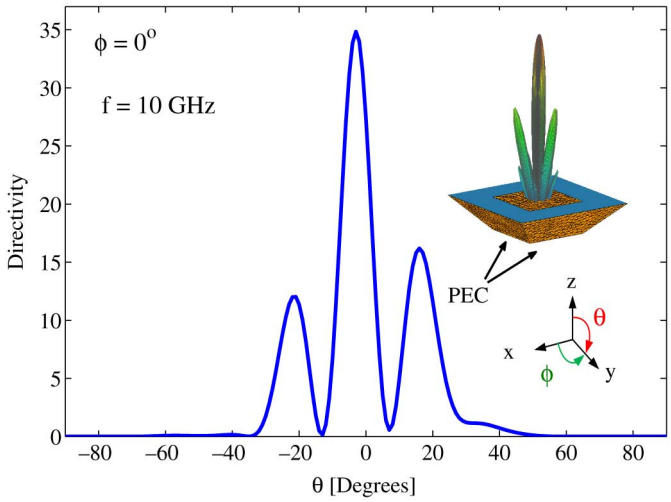


Fig. 4. Simulated directivity of the sum pattern assuming an ideal ENZ block.

shown in Fig. 5(a) or (b) and the radiation pattern is as shown in Figs. 4 or 5. The size of the ENZ block is another degree of freedom in controlling the radiation pattern. For example, as the $xy$ size of the ENZ block in Fig. 2 increases, the null of the difference pattern becomes sharper. Equivalently, gain increases and the four lobes become closer to each other. Furthermore, as the $xy$ size of the ENZ block increases, the sum pattern beam angle becomes closer to $\theta = 0$.

Figs. 3–5 are obtained by simulation [29] of a structure with the following flare size: the bottom rectangle is $8 \times 8\,\mathrm{cm}$, the upper rectangle is $16 \times 16\,\mathrm{cm}$, and the angle is 45°. The dielectric flare material surrounding the ENZ block has permittivity 3.84 (plaster material), the frequency is 10 GHz, and the monopole antenna length is 7.5 mm. These simulations have been done using a wire monopole with zero thickness and an ideal ENZ block. Although the purpose of these examples is to demonstrate the capabilities of mixing the TIR and PEC reflections, it can be noted that the sum and difference patterns [28] are similar to what is used in tracking systems. In a tracking system, the difference pattern of a steerable antenna is used to lock the target in the null of the pattern. There are several

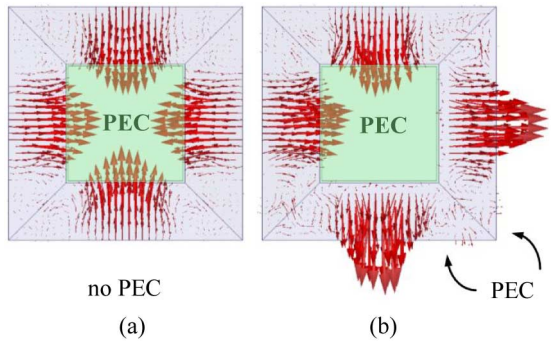


Fig. 5. Simulated electric field distribution on the radiating surface assuming an ideal ENZ block.

well known realizations for sum and difference patterns such as Taylor and Bayliss distributions, which use phased arrays with complex feed networks [30]–[33].

The four radiating apertures in Fig. 5 can be seen as two arrays of two elements, rotated one from another by 90°. Therefore, it is fairly straight forward to find the array factor of the structure. For the two apertures on the $x$-axis, the array factor of $E_\theta$ in the far field is [34]

$$AF_{\mathrm{x}}^{\theta} = 1 + \exp\left(j\varphi_{\mathrm{x}} + jk\sin\left(\theta_{\mathrm{x}}\right)\right) \tag{8}$$

where $k$ is the wavenumber, $d$ is the spacing between the elements, $\varphi_{\mathrm{x}}$ is the phase difference between the elements, and $\theta_{\mathrm{x}}$ is the angle between the $z$- and the $x$-axes, as indicated in Fig. 2. Similarly, the $E_\theta$ array factor of the two apertures on the $y$-axis is

$$AF_{\mathrm{y}}^{\theta} = 1 + \exp\left(j\varphi_{\mathrm{y}} + jk\sin\left(\theta_{\mathrm{y}}\right)\right) \tag{9}$$

in which $\varphi_{\mathrm{y}}$ is the phase difference between the apertures, and $\theta_{\mathrm{y}}$ is the angle between the $z$- and the $y$-axes. Note that in Fig. 5(a) and (b), $\varphi_{\mathrm{x}}$ and $\varphi_{\mathrm{x}}$ are both equal to $\pi$ and zero, respectively. We have used the angle set $(\theta_{\mathrm{x}}, \theta_{\mathrm{y}})$ instead of the conventional spherical coordinate angles, $(\varphi, \theta)$, since it leads to simpler equations for our purpose. Then, the $z$- and the radial (parallel to $xy$ plane) components of the array factors are

$$AF_{\mathrm{x,y}}^{z} = -AF_{\mathrm{x,y}}^{\theta} \times \sin\left(\theta_{\mathrm{x,y}}\right), \quad AF_{\mathrm{x,y}}^{\rho} = AF^{\theta} \times \cos\left(\theta_{\mathrm{x,y}}\right). \tag{10}$$

Therefore, the total $z$-component of the structure's array factor is

$$AF_{\mathrm{t}}^{z} = -AF_{\mathrm{x}}^{\theta} \times \sin\left(\theta_{\mathrm{x}}\right) - AF_{\mathrm{y}}^{\theta} \times \sin\left(\theta_{\mathrm{y}}\right). \tag{11}$$

Similarly, we can find the radial component of the structure's array factor $(AF_{\mathrm{t}}^{\rho})$. However, we should note that the currents of the apertures on the $x$- and the $y$-axes (and therefore their array factor's radial components) have 90° orientation difference. Hence,

$$\begin{aligned} AF_{\mathrm{t}}^{\rho} &= \sqrt{\left(AF_{x}^{\rho}\right)^2 + \left(AF_{y}^{\rho}\right)^2} \\ &= \sqrt{\left(AF_{\mathrm{x}}^{\theta} \times \cos\left(\theta_{\mathrm{x}}\right)\right)^2 + \left(AF_{\mathrm{y}}^{\theta} \times \cos\left(\theta_{\mathrm{y}}\right)\right)^2}. \end{aligned} \tag{12}$$

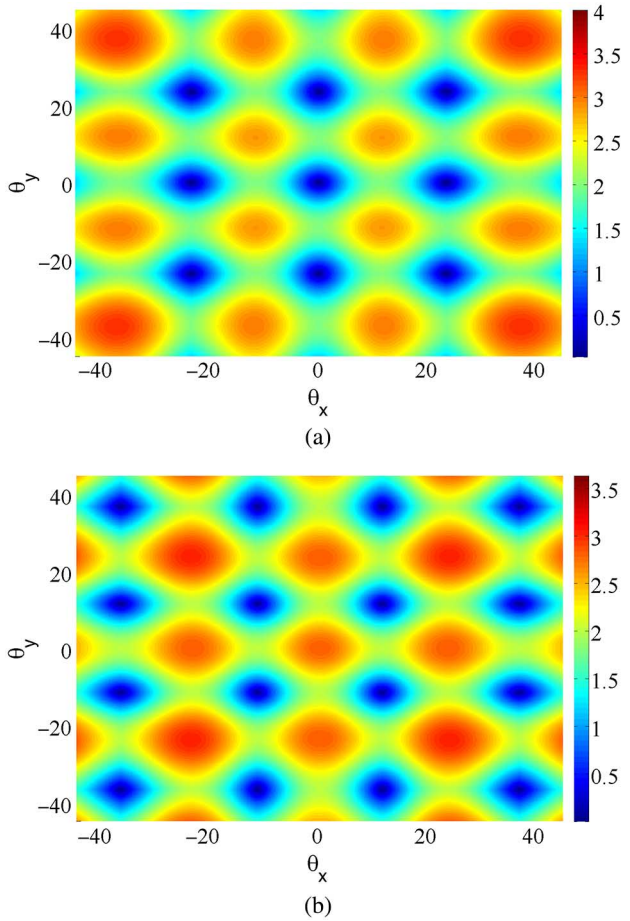


Fig. 6. Array factors of $E_\theta$ for: (a) array of Fig. 5(a); and (b) array of Fig. 5(b).

Finally, the total $E_\theta$ array factor of the structure is

$$AF_{\mathrm{t}}^{\theta} = \sqrt{\left(AF_{\mathrm{t}}^{\rho}\right)^2 + \left(AF_{\mathrm{t}}^{z}\right)^2}. \tag{13}$$

As an example, Fig. 6 shows the array factors of the structures of Fig. 5, for the separation $d = 2.5\lambda$ (which is the approximate separation in the fabricated antenna in this paper), leading to sum and difference patterns. Obviously, the element factor (radiation pattern of the aperture) should be multiplied to the array factor to find the total sum and difference patterns. As is clear from Fig. 6, the separation between radiating edges for the designed antenna ($d = 2.5\lambda$) leads to multiple grating lobes. In fact, the main lobes of the array factor are located at large angles ($>20°$) where they cannot contribute to the overall radiation pattern due to the directive element factor (by the aperture). As will be seen later in this paper, the lobes of the array factor at small angles (below 20°) will be important in the total radiation pattern of the fabricated antenna due to the directivity of the element pattern. Choosing a smaller separation would lead to a larger directivity, would remove the grating lobes, and would shift the main lobes of the array factor to smaller angles. But, practically, the separation between the apertures has to be large enough to be able to fit enough wires in the ENZ block and has a valid homogenized model for WM. With the chosen $d = 2.5\lambda$, we were able to accommodate 12 wires in the fabricated ENZ block, as will be discussed later in this paper.

Having described the antenna idea, in the next two sections we validate first the ENZ block portion of the antenna using fullwave simulations of the WM, and then the full antenna results are presented.

## III. ENZ Block

Due to the advent of three-dimensional (3-D) printers, it is quite easy to fabricate structures as in Fig. 2. We chose to sectionize the geometry into a WM block section and a dielectric flare section and fabricate them separately. This allowed us to measure the exact frequency at which the ENZ condition occurs by comparing the radiation pattern of the ENZ block with an ideal ENZ block at different frequencies. The fabricated ENZ block consisted of a $12 \times 12$ array of parallel wires forming a uniaxial WM. The period, diameter, and length of the wires were 6, 1.2, and 40 mm, respectively. The wires were stripped TP1109-Y-1W06 jumper wires. The dielectric material supporting the wires was a plastic material (ABS-plus) which was a typical insulating material used by 3-D printers. The relative permittivity of the plastic was measured using a split post dielectric resonator (SPDR) [35] to be 2.25. The plastic block with holes was 3-D printed, and then the wires were inserted in the holes.

Equation (2) predicts a plasma frequency of 13.6 GHz for the designed WM. However, since strong spatial dispersion is expected, and since the near field of the monopole feed excites both transverse and longitudinal components (although the transverse wave will dominate in the far field), it is expected that the ENZ condition will occur in a range between the nonlocal predications (5) and (6), associated with pure transverse and longitudinal excitations, respectively [24]. For the fabricated geometry, (5) predicts that the ENZ condition will occur at 9.1 GHz, and (6) yields 11.1 GHz (assuming $l_0 = 3$), so we expect that the fabricated, monopole-fed WM will exhibit ENZ behavior somewhere in the range 9.1–11.1 GHz. As we show next, the measured ENZ behavior is observed near 10.5 GHz, within the expected range from the nonlocal model and well below the plasma frequency based on (2). Although (5) and (6) are derived for an isotropic WM, it is a good approximation to use them for the uniaxial WM in our ENZ block, because the electric field in the block is mostly $z$ directed (parallel to the wires). Therefore, the existence/absence of wire sets in the $x$ and $y$ directions is not very important. Note that, at the ENZ frequency, only normal radiation from the lateral sides of the uniaxial WM cube is possible (similar to a cube made of isotropic WM). In fact, a source in uniaxial WM can excite two different propagating waves.

1) Ordinary TEM waves with the electric field perpendicular to both the anisotropy axis (along the wires) and the wave vector, which can only propagate along the wires. These waves neither can be excited nor can contribute to radiation because of the metal caps on both sides of the wire (the metal caps prevent $q_z = \omega\sqrt{\varepsilon_h \mu_0}$ which is the required condition for these waves. $q_z$ is the $z$-component of the wave vector, and $\varepsilon_h$ is the host permittivity of WM).

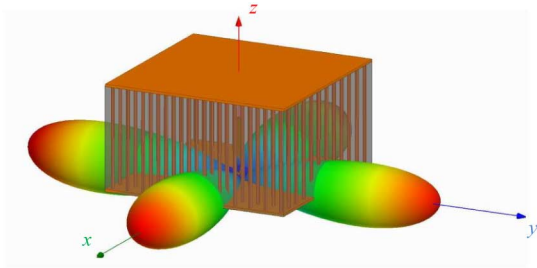


Fig. 7. Expected radiation pattern of the WM at the ENZ frequency.

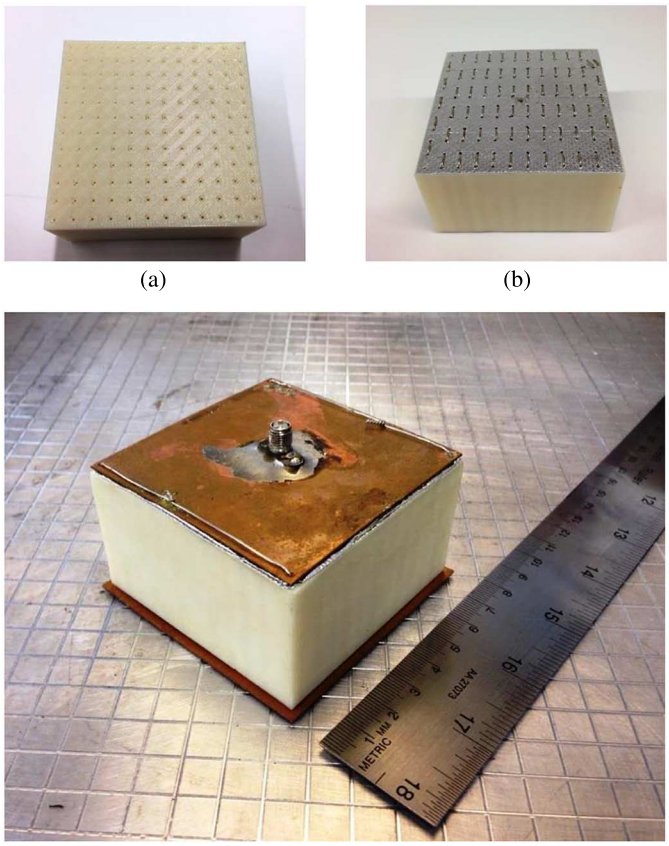


Fig. 8. Fabricated ENZ block. (a) 3-D printed dielectric block having holes to inhibit wires; (b) with wires installed; (c) after installing the feed and metal caps.

2) Extraordinary TM waves with the magnetic field perpendicular to the wires with the dispersion equation

$$\mathbf{q}^2 = \mu_0 \left(\varepsilon_h \omega^2 - \varepsilon_0 \omega_{\rm p}^2\right) \tag{14}$$

in which $\mathbf{q}$ is the wave vector, $\omega_{\rm p}$ is the plasma radial frequency, and $\varepsilon_h$ is the host permittivity of the WM. Because of the metal caps on two sides of the cube, $q_z^2 \leq 0$. For the case $q_z = 0$ (which means a uniform wave in $z$-direction), (14) forces the propagating waves in $x$- and $y$- directions to have both $q_x = 0$ and $q_y = 0$ at $\omega = \omega_{\rm p}/\sqrt{\varepsilon_{\rm h}}$. This is in fact a transverse wave which propagates to the lateral sides of the cube with no delay (i.e., ENZ condition) and, as expected, its ENZ condition is the same as (5). It can be easily seen from (14) that for higher order modes (i.e., $q_z^2 < 0$), $q_x$ and $q_y$ cannot become zero simultaneously at $\omega = \omega_{\rm p}/\sqrt{\varepsilon_{\rm h}}$.

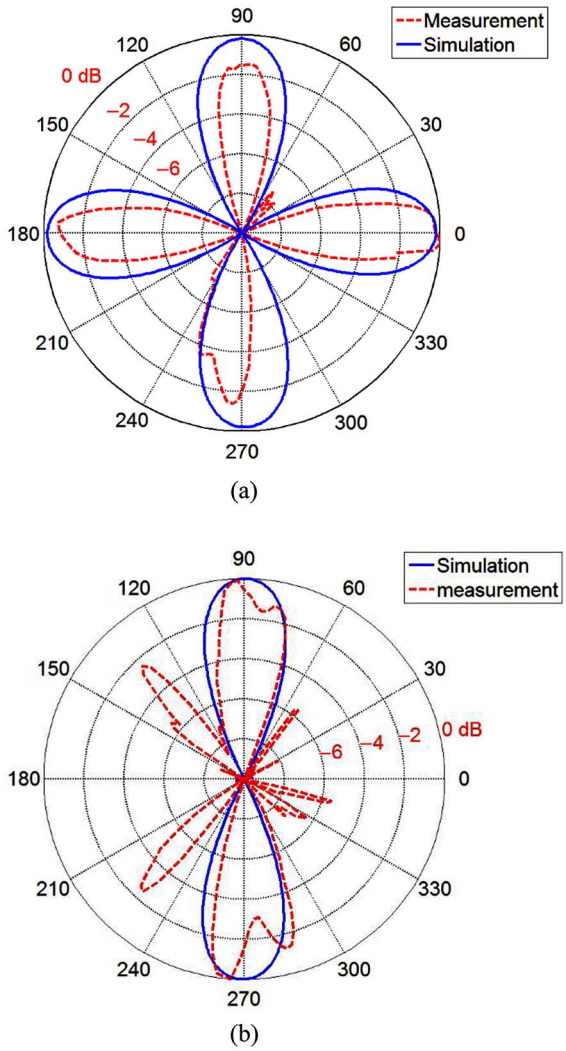


Fig. 9. Measured and full wave simulated radiation pattern $E_\theta$ of the ENZ block for: (a) $\theta = 90$, $0 < \phi < 360$; and (b) $\phi = 0$, $0 < \theta < 360$.

Fig. 7 shows the expected radiation pattern of the WM block at the ENZ frequency. Two metal caps on on top and bottom block faces confine the radiation to the lateral sides. At the same time, they provide more mechanical strength (especially for the feed) and one of them serves as the ground plane for the feed as well. The feed monopole has a length of 12 mm.

Fig. 8 shows the fabricated ENZ block. As shown in Fig. 9, the measured pattern of the WM block is in acceptable agreement with the expected radiation pattern of an ideal ENZ block (i.e., four lobes normal to the lateral sides of the block) at 10.5 GHz.

Using transmission line theory, a monopole antenna placed inside a layer of ENZ material sees an effective intrinsic impedance ($\eta_{\rm in}$)

$$\begin{aligned}\eta_{\rm in} &= \lim_{\varepsilon \to 0} \left(\eta_{\rm ENZ} \frac{\eta_0 + j\eta_{\rm ENZ} \tan\left(k_{\rm ENZ} L\right)}{\eta_{\rm ENZ} + j\eta_0 \tan\left(k_{\rm ENZ} L\right)}\right) \\ &= \eta_0 \left(1 + j\omega k_0 L\right)\end{aligned} \tag{15}$$

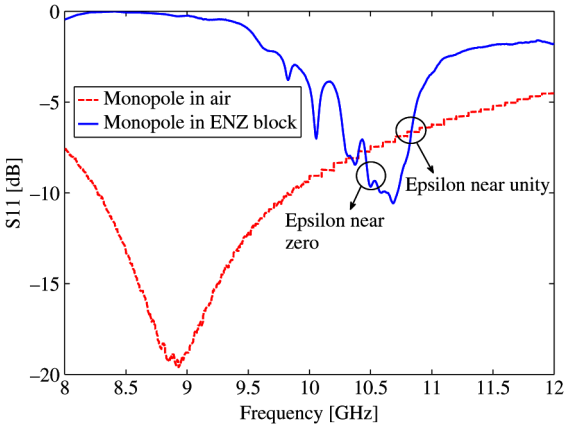


Fig. 10. Measure $S_{11}$ of the fabricated ENZ block and of the same monopole in free space.

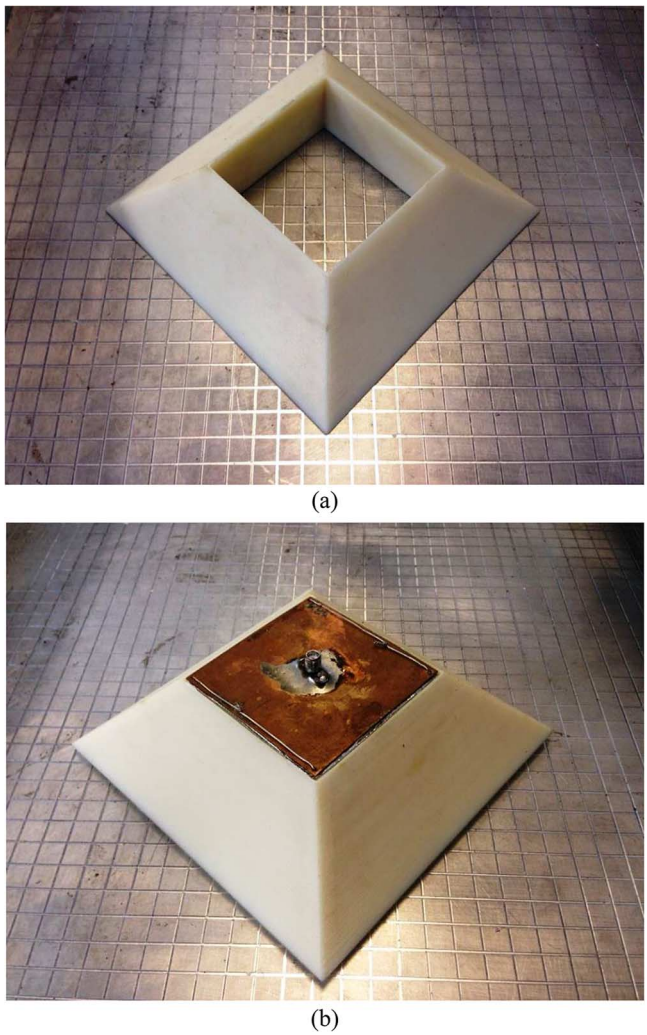


Fig. 11. (a) Fabricated dielectric flare. (b) Complete antenna including the ENZ block and the dielectric flare.

where $\eta = \sqrt{\mu/\varepsilon}$ is the intrinsic impedance, $\mu$ is the permeability, $\varepsilon$ is the permittivity, $k$ is the wave number, and $L$ is the length of the ENZ layer. The subscripts 0 and ENZ denote air and the ENZ layer, respectively. Therefore, the monopole in Fig. 8 sees $\eta_{\text{in}} = \eta_0(1 + j8.79)$ as the surrounding intrinsic

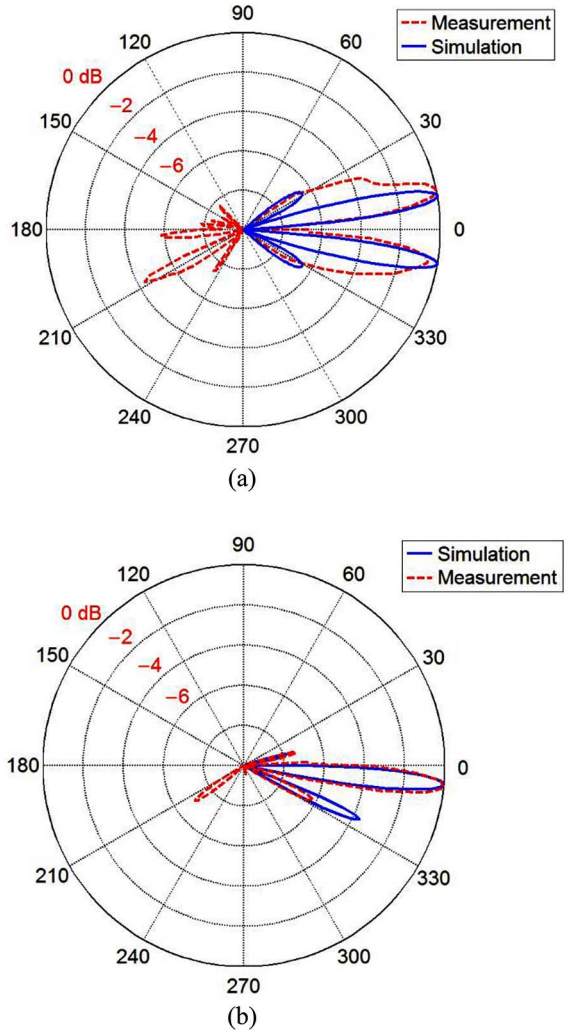


Fig. 12. Measured and full wave simulated radiation pattern $E_\theta$ of the antenna: (a) difference pattern; and (b) sum pattern.

impedance (since $L = 4\,\text{cm}$ and $f = 10.5\,\text{GHz}$). The measured input characteristic (S11) of the block is shown in Fig. 10. The ENZ frequency (10.5 GHz) and epsilon near unity frequency (10.9 GHz) are specified in Fig. 10. At the ENZ frequency, the monopole has a marginally smaller reflection than the monopole in air due to the scaling of intrinsic impedance by the ENZ layer.

## IV. Measured Antenna Results

By adding the 3-D printed dielectric flare to the fabricated WM block, the proposed antenna of Section II has been realized as shown in Fig. 11. Then, placing/removing two PEC covers on the side walls of the flare will provide the expected sum/difference pattern. Fig. 12 shows the normalized simulated and measured difference and sum patterns of the fabricated geometry (simulations have been done in HFSS [36]), which show good agreement with the expected results. We believe the discrepancies seen between the simulation and the measurement results are mainly due to the fabrication inaccuracies. This can be seen from the nonsymmetrical radiation pattern of the ENZ cube in Fig. 9(a). Also, the ground plane does not have

a perfect contact with wires (it needed 144 holes to be drilled in it for good connection) and is causing some unwanted lobes in Fig. 9(b). The simulations in this section (Figs. 9 and 12) are performed assuming the actual $12 \times 12$ wire array forming the WM (in contrast to Figs. 3–5 in which an ideal ENZ block was used).

Note that although the null in the difference pattern is exactly located at $\theta = 0°$, the main beam of the sum pattern is at $\theta = 7°$. The half power beam width (HPBW) of the difference and sum patterns are 4° and 20°, respectively. The change in the input characteristic of the antenna with and without the flare section is not noticeable and remains the same as in Fig. 10.

## V. Conclusion

An antenna geometry was proposed based on the TIR principle, and the concept of ENZ materials, to control the radiation pattern. The antenna consists of a cubical ENZ material surrounded by a dielectric flare and fed by a monopole. The ENZ material was realized using a uniaxial WM. Two different radiation patterns, sum and difference patterns, were realized by placing different arrangements of conductive sheets on the side walls of the flare. The antenna was built using a 3-D printer and measured, and good agreement was found between theory and experiment.

## Acknowledgment

The authors would like to thank J. Kovits at UCLA for his help in measuring the first fabricated sample.

## References

[1] D. Axelrod, "Cell-substrate contacts illuminated by total internal reflection fluorescence," *J. Cell Biol.*, vol. 89, no. 1, pp. 141–145, Apr. 1981.

[2] R. Ehrlich, *Why Toast Lands Jelly-Side Down: Zen and the Art of Physics Demonstrations*. Princeton, NJ, USA: Princeton Univ. Press, 1997, p. 182.

[3] R. M. Knox, "Dielectric waveguide microwave integrated circuits–An overview," *IEEE Trans. Microw. Theory Tech.*, vol. 24, pp. 806–814, Nov. 1976.

[4] D. Kajfez and P. Guillon, *Dielectric Resonators*. Norwood, MA, USA: Artech House, Inc., 1986.

[5] J. A. Pierce and H. R. Mimno, "The reception of radio echoes from distant ionospheric irregularities," *Phys. Rev.*, vol. 57, no. 2, p. 95, 1940.

[6] M. G. Silveirinha and N. Engheta, "Tunneling of electromagnetic energy through sub-wavelength channels and bends using $\varepsilon$-near-zero materials," *Phys. Rev. Lett.*, vol, 97, no. 15, p. 157403, 2006.

[7] S. Enoch, G. Tayeb, P. Sabouroux, N. Guerin, and P. Vincent, "A metamaterial for directive emission," *Phys. Rev. Lett.*, vol. 89, no. 21, p. 213902, 2002.

[8] B. Wang and K. Huang, "Shaping the radiation pattern with mu and epsilon-near-zero metamaterials." *Prog. Electromagn. Res.*, vol. 106, pp. 107–119, 2010.

[9] A. Alu, M. G. Silveirinha, A. Salandrino, and N. Engheta, "Epsilon-near-zero metamaterials and electromagnetic sources: Tailoring the radiation phase pattern," *Phys. Rev. B*, vol. 75, no. 15, p. 155410, 2007.

[10] R. W. Ziolkowski, "Propagation in and scattering from a matched metamaterial having a zero index of refraction," *Phys. Rev. E*, vol. 70, no. 4, p. 046608, 2004.

[11] H. Zhou *et al.*, "A planar zero-index metamaterial for directive emission," *J. Electromagn. Waves Appl.*, vol. 23, no. 7, pp. 953–962, 2009.

[12] V. Mocella, P. Dardano, I Rendina, and S. Cabrini, "An extraordinary directive radiation based on optical antimatter at near infrared," *Opt. Express*, vol. 18, no. 24 pp. 25068–25074, 2010.

[13] Y. G. Ma, P. Wang, X. Chen, and C. K. Ong, "Near-field plane-wave-like beam emitting antenna fabricated by anisotropic metamaterial," *Appl. Phys. Lett.*, vol. 94, no. 4, p. 044107, 2009.

[14] Q. Wu, P. Pan, F. Y. L. Meng, W. Li, and J. Wu, "A novel flat lens horn antenna designed based on zero refraction principle of metamaterials," *Appl. Phys. A*, vol. 87, pp. 151–156, 2007.

[15] Y. Yu, L. F. Shen, L. X. Ran, T. Jiang, and J. T. Huangfu, "Directive emission based on anisotropic metamaterials," *Phys. Rev. A*, vol. 77, p. 053821, 2008.

[16] J. Yang, M. Huang, and J. Peng "Directive emission obtained by Mu and epsilon-near-zero metamaterials," *Radio Eng. J.*, vol. 18, pp. 124–128, 2009.

[17] R. Zhou, H, Zhang, and Hao Xin, "Metallic wire array as low-effective index of refraction medium for directive antenna application," *IEEE Trans. Antennas Propag.* vol. 58, no. 1, pp. 79–87, Jan. 2010.

[18] P. Drude, "Zur Elektronentheorie der metalle," *Ann. Phys.*, vol. 306, no. 3, p. 566, 1900.

[19] P. A. Belov *et al.*, "Strong spatial dispersion in wire media in the very large wavelength limit," *Phys. Rev. B*, vol. 67, no. 11, p. 113103, 2003.

[20] M. G. Silveirinha, "Artificial plasma formed by connected metallic wires at infrared frequencies," *Phys. Rev. B*, vol. 79, p. 035118 (1)–035118 (15), 2009.

[21] M. G. Silveirinha and C. A. Fernandes, "Homogenization of 3-D-connected and nonconnected wire metamaterials," *IEEE Trans. Microw. Theory Tech.*, vol. 53, no. 4, pp. 1418–1430, Apr. 2005.

[22] S. I. Maslovski and M. G. Silveirinha, "Nonlocal permittivity from a quasistatic model for a class of wire media," *Phys. Rev B*, vol. 80, pp. 245101 (1)–245101 (10), 2009.

[23] G. W. Hanson, E. Forati, and M. G. Silveirinha, "Modeling of spatially-dispersive wire media: Transport representation, comparison with natural materials, and additional boundary conditions," *IEEE Trans. Antennas Propag.*, vol. 60, no. 9, pp. 4219–4232, Sep. 2012.

[24] E. Forati and G. W. Hanson, "On the epsilon near zero condition for spatially dispersive materials," *New J. Phys.*, vol. 15, no. 12 p. 123027, 2013.

[25] M. G. Silveirinha and A. B. Yakovlev, "Negative refraction by a uniaxial wire medium with suppressed spatial dispersion," *Phys. Rev. B*, vol. 81, no. 23, p. 233105, 2010.

[26] G. W. Hanson, M. G. Silveirinha, P. Burghignoli, and A. B. Yakovlev, "Non-local susceptibility of the wire medium in the spatial domain considering material boundaries," *New J. Phys.*, vol. 15, no. 8, p. 083018, 2013.

[27] M. G. Silveirinha and S. I. Maslovski, "Radiation from elementary sources in a uniaxial wire medium," *Phys. Rev. B*, vol. 85, no. 15, p. 155125, 2012.

[28] M. I. Skolnik, *Radar Handbook*. New York, NY, USA: McGraw-Hill, 1970.

[29] *FEKO Electromagnetics Comprehensive Solutions* [Online]. Available: www.feko.info

[30] R. C. Hansen, *Phased Array Antennas*. Hoboken, NJ, USA: John Wiley and Sons, Inc., 1998.

[31] M. D'Urso and T. Isemia, "Solving some array synthesis problems by means of an effective hybrid approach," *IEEE Trans. Antennas Propag.*, vol. 55, no. 3, pp. 750–759, Mar. 2007.

[32] L. Manica, P. Rocca, A. Martini, and A. Massa, "An innovative approach based on a tree-searching algorithm for the optimal matching of independently optimum sum and difference excitations," *IEEE Trans. Antennas Propag.*, vol. 56, no. 1, pp. 58–66, Jan. 2008.

[33] H. Oraizi and M. Fallahpour, "Sum, difference and shaped beam pattern synthesis by non-uniform spacing and phase control," *IEEE Trans. Antennas Propag.*, vol. 59, no. 12, pp. 4505–4511, Dec. 2011.

[34] W. L. Stutzman and W. A. Davis, *Antenna Theory*, Hoboken, NJ, USA: Wiley, 1998.

[35] QWED Inc. Warsaw, Poland. [Online]. Available: www.qwed.com.pl

[36] Ansys HFSS [Online]. Available: www.ansys.com

**Ebrahim Forati** (GSM'09) was born in Iran in 1983. He received the B.Sc. and M.Sc degrees from Iran University of Science and Technology (IUST), Tehran, Iran, and the Ph.D. degree from the University of Wisconsin Milwaukee (UWM), Milwaukee, WI, USA, in 2006, 2009, and 2014, respectively.

From 2014, he is a Postdoc Researcher with the Applied Electromagnetics Group, University of California, San Diego, CA, USA, where he is focused on metasurface based micro-plasma devices and microfabrication.

**George W. Hanson** (S'85–M'91–SM'98–F'09) was born in Glen Ridge, New Jersey, in 1963. He received the B.S.E.E. degree from Lehigh University, Bethlehem, PA, USA, the M.S.E.E. degree from Southern Methodist University, Dallas, TX, USA, and the Ph.D. degree from Michigan State University, East Lansing, MI, USA, in 1986, 1988, and 1991, respectively.

From 1986 to 1988, he was a Development Engineer with the General Dynamics, Fort Worth, TX, USA, where he worked on radar simulators. From 1988 to 1991, he was a Research and Teaching Assistant with the Department of Electrical Engineering, Michigan State University. He is currently a Professor of electrical engineering and computer science with the University of Wisconsin, Milwaukee, WI, USA. He is the coauthor of the book *Operator Theory for Electromagnetics: An Introduction* (Springer, 2002), and the author of *Fundamentals of Nanoelectronics* (Prentice-Hall, 2007). His research interests include nanoelectromagnetics, quantum optics, mathematical methods in electromagnetics, and electromagnetic wave phenomena in layered media.

Dr. Hanson is a member of URSI Commission B, Sigma Xi, and Eta Kappa Nu. He was an Associate Editor for the IEEE TRANSACTIONS ON ANTENNAS AND PROPAGATION from 2002 to 2007. In 2006, he received the S.A. Schelkunoff Best Paper Award from the IEEE Antennas and Propagation Society.

**Daniel F. Sievenpiper** (M'94–SM'04–F'09) received the B.S. and Ph.D. degrees in electrical engineering from the University of California, Los Angeles, USA, in 1994 and 1999, respectively.

He is currently a Professor with the University of California, San Diego, CA, USA, where his research focuses on antennas and electromagnetic structures. Prior to 2010, he was the Director of the Applied Electromagnetics Laboratory with the HRL Laboratories, Malibu, CA, USA. He has more than 70 issued patents and more than 80 technical publications. His research interests include artificial impedance surfaces, conformal antennas, tunable and wearable antennas, and beam steering methods.

Dr. Sievenpiper has served as an Associate Editor of IEEE ANTENNAS AND WIRELESS PROPAGATION LETTERS, since 2010. He currently serves as the Chair of the IEEE Antennas and Propagation Society Committee on New Technology Directions. He was awarded the URSI Issac Koga Gold Medalm, in 2008.